crystals

MDPI

Article

A Study on Metallographic and Machining Characteristics of Functionally Graded Material Produced by Directed Energy Deposition

Inwoong Noh [1], **Jaehun Jeon** [2] **and Sang Won Lee** [3,*]

[1] Department of Mechanical Engineering, Sungkyunkwan University, Suwon 16419, Republic of Korea
[2] Samsung Electro-Mechanics Co., Ltd., Suwon 16674, Republic of Korea
[3] School of Mechanical Engineering, Sungkyunkwan University, Suwon 16419, Republic of Korea
* Correspondence: sangwonl@skku.edu

Abstract: Directed energy deposition (DED) stands as a key process in metal additive manufacturing (AM) and offers the unique capability of creating functionally graded materials (FGMs). FGMs have garnered significant interest in high-value industries by advantages such as performance optimization, reducing material defects, and resolving joining issues. However, post-processing remains a crucial step, indicating a need for further research to understand the machinability of FGMs. This paper focuses on the characteristics analysis of fabricating and machining an FGM based on stainless steel 316L (SAE 316L) and Inconel 718. The FGM was fabricated by starting with SAE 316L at 100 wt.% and adjusting the composition ratio by incrementally increasing Inconel 718 by 20 wt.% while simultaneously decreasing SAE 316L. Following the FGM fabrication, microstructure and mechanical properties were comprehensively analyzed by hardness testing, optical microstructure measurements, energy dispersive spectroscopy (EDS), and X-ray diffraction (XRD). To investigate the post-processing aspects, end-milling experiments were conducted using two distinct milling methods (upward and downward milling) and machining paths (from SAE 316L towards Inconel 718, and vice versa). The mean cutting force peaked at 148.4 N in upward milling and dipped to 70.5 N in downward milling, and tool wear measurements further provided insights into the optimal milling direction when working with an FGM of SAE 316L and Inconel 718.

Keywords: directed energy deposition; functionally graded material; microstructure analysis; microhardness testing; post-machining

Citation: Noh, I.; Jeon, J.; Lee, S.W. A Study on Metallographic and Machining Characteristics of Functionally Graded Material Produced by Directed Energy Deposition. *Crystals* **2023**, *13*, 1491. https://doi.org/10.3390/cryst13101491

Academic Editor: Umberto Prisco

Received: 17 September 2023
Revised: 6 October 2023
Accepted: 10 October 2023
Published: 13 October 2023

1. Introduction

Additive manufacturing (AM) is a technology that is used to fabricate a product in a layer-by-layer fashion, using resin, polymer, and metal materials, which is advantageous for complex designs [1–5]. Particularly, directed energy deposition (DED), one of representative metal AM processes, is a process in which a metal powder or wire is deposited on another material with a high-energy heat source such as laser, electron beam, plasma, and so on. Consequently, metal structures are fabricated by melting and solidification, which makes it possible to manufacture high-density and high-strength products [6,7]. Furthermore, compared to the powder bed fusion (PBF) process, DED offers a greater level of flexibility, particularly in handling a wide range of materials and reduced size constraints, and can be applied to pre-existing parts. This enables effective utilization of DED for the production or repair of parts with intricate geometries. The most notable advantage of the DED process is the ability to create functionally graded materials (FGMs) by combining two or more materials in variable proportions.

An FGM is a heterogeneous composite manufactured by a gradual change in the composition of dissimilar materials to compensate for catastrophic defects resulting from abrupt changes in the thermal/physical properties at the interface and differences in the mechanical properties of the metal materials. A gradual change in the composition of dissimilar metals in such an FGM allows the microstructure to compensate for corrosion and cracking caused by dissimilar metal bonds. Therefore, due to such compensation, FGMs can be utilized in a variety of industries, such as automotive, nuclear power, and aerospace sectors. In response to the demand for such materials, functionally graded additive manufacturing (FGAM), which fabricates FGMs using metal AM, has recently gained attention [8–10].

The fabrication of FGMs has been studied using a variety of difficult-to-cut materials to obtain unique properties, with a focus on their microstructure and mechanical properties [11–13]. The fabrication of FGMs using FGAM, particularly with stainless steel and Inconel alloys, has garnered significant attention due to their potential applications in high-value industries. These alloys have exceptional mechanical and chemical properties, such as resilience in high-temperature hazard environments, corrosion resistance, and superior strength [14]. Generally, to evaluate the quality and integrity of deposited layers, researchers have assessed the correlation between the microstructure and measured mechanical properties [15,16]. This method provided insight into whether the parts were deposited without defects and addressed specific challenges such as galvanic corrosion or stress fractures that can arise from the differences in thermal expansion coefficients during direct joining or welding between stainless steel and Inconel alloys. Su et al. fabricated an FGM using SAE 316L and Inconel 718 alloy in three different composition ratios through laser metal deposition (LMD). Microscopy, EDS, XRD, and tensile tests were applied to examine the microstructure, phase evolution, and mechanical properties of FGMs [17]. In a similar study, Zhang et al. performed a microstructural analysis showing that the intermediate section between SAE 316L and Inconel 625 was layered without defects. They also analyzed fracture morphology using tensile tests [18]. Rodrigues et al. utilized a dual-wire arc AM method instead of powder-based AM to fabricate an FGM with continuous compositional transition between stainless steel 316L and Inconel 625. Through this system, they observed smooth microstructural transition and analyzed the correlation between microstructures and mechanical properties by producing four different specimens: 100% of each material, a direct interface composite, and an FGM [19]. Similarly, Yu et al. evaluated the mechanical properties of an FGM fabricated from the same materials in both vertical and horizontal directions and analyzed their correlation with the microstructure [20]. Based on the microstructural analysis and mechanical property measurements to verity that the FGM was properly fabricated, Kim et al. also fabricated an FGM using SAE 316L and Inconel 718, which varied in steps of 10 wt.% for each layer, and analyzed the microstructural and mechanical properties of the layers with critical pores and fractures [21]. Based on the dual-wire arc AM system, Li et al. analyzed cracks in an FGM and solve the crack issue by process parameter optimization [22]. Yang et al. fabricated nongraded, 25% graded, and 10% graded FGMs. Using SEM imaging, they identified cracks not only at the interface of the nongraded sample but also at specific mixing ratios in the graded samples. Their analysis revealed that the cracks were caused by the differences in the coefficient of thermal expansion and precipitation of components such as Nb and Mo [23]. Additionally, from the perspective of predicting microstructures through a thermodynamic model, Carroll et al. produced an FGM by progressively increasing and decreasing the composition ratio of 4% using SAE 304L and Inconel 625 alloys. After depositing the FGM, the microstructure, chemical composition, phase composition, and microhardness were analyzed using the CALculation of PHAse Diagrams (CALPHAD) method, and the composition variation area was predicted [24]. Previous studies not only validated the proper gradual formation of FGMs through microstructural analysis but also assessed the absence of defects at the interface. Furthermore, by analyzing the differences in the mechanical properties between the wrought material and the deposited material, the potential for practical application in industry was verified.

In the meantime, to apply the FGMs in industry, machining is essential for improving surface roughness and dimensional accuracy after the DED part fabrication. To fulfill these requirements, the machinability of each material, such as cutting force and tool life, must be initially assessed [25–27]. Likewise, the machinability of the graded sections in the FGM part should also be thoroughly analyzed. However, there are few studies on the experimental analysis on characteristics of the post-machining of deposited FGMs. Oyelola et al. investigated the machining characteristics of functionally graded Ti6Al4V/WC components consisting of a metal matrix composite (MMC) region and a single alloy region produced by a turning process. According to material variations of the functionally graded components, the cutting force, tool wear, and surface integrity were analyzed [28]. Levano Blanch et al. fabricated a special billet from four different titanium alloys, and face-turning was performed to collect the cutting force across diffusion bonds. Based on the cutting force and microstructure of diffusion bonds between titanium alloys, the machinability of titanium alloys was analyzed for application in the aerospace industry [29]. Compared to the turning process, the milling process is more suitable for ensuring the surface roughness and precision of the deposited FGM. In research geared towards analyzing the machinability of FGMs for the milling process, Wang et al. fabricated an FGM based on stainless steel 304L and Inconel 625 through a 25% increment–decrement approach and using a 4-flute cemented carbide tool. The tool wear was analyzed based on two objectives, minimum milling force and surface roughness, which led to the selection of an appropriate machining strategy [30]. However, given the various strategies available, such as the sequence of material processing and the specific milling method, further research is needed to explore the best strategy for FGM machining.

Considering the recent research trends in FGMs, such as the potential significance of FGMs for high-value industries grows, there has been active research to characterize FGMs in terms of their microstructure and mechanical properties. Nonetheless, despite the crucial nature of post-machining for enhancing surface quality and dimensional accuracy, there has been limited investigation into FGMs' machining characteristics.

In this study, an FGM composed of SAE 316L and Inconel 718 with a progressively varying composition ratio was additively manufactured in a hybrid DED machine tool, and its microstructures, mechanical properties, and machining characteristics were experimentally investigated. In more detail, after making the FGM specimens, their microstructural and mechanical properties were investigated experimentally. Then, a series of milling experiments were conducted, and cutting force and tool wear analyses were performed in accordance with milling directions and milling passes.

2. DED for FGM Experiments

2.1. Powders

For the fabrication of the FGM, gas-atomized SAE 316L powder (MetCoclad 316L-Si, Oerlikon Metco, Pfäffikon, Switzerland) and Inconel 718 powder (MetCoclad 718, Oerlikon Metco, Pfäffikon, Switzerland) were selected. Due to its high yield and tensile strengths, corrosion resistance, and weldability, austenitic stainless steel SAE 316L has been used in a variety of subtractive and additive manufacturing processes [31]. The austenitic nickel–chromium-based superalloy, Inconel 718, which is resistant to thermal oxidation and corrosion, has typically been used as an additive manufacturing material in high-value-added industries [32]. In addition, AISI 1045 carbon steel was chosen as the substrate for the DED process, and the constituents of the powders and substrate are listed in Table 1. The dimensions of the SAE 316L powder ranged between 44 and 106 µm, and those of the Inconel 718 powder ranged between 45 and 90 µm, as confirmed by the supplier's data.

Table 1. The material constituents of powders and substrate.

Element (wt.%)	Fe	Ni	Cr	Mn	Si	C	Mo	Nb	Ti	Others
SAE 316L powder	Bal.	12	17	2.3	2.3	0.03	-	-	-	$\leq$0.5
Inconel 718 powder	18	Bal.	19	-	-	-	3	5	1	$\leq$1.0
AISI 1045 substrate	Bal.	-	-	-	0.7	0.45	-	-	-	-

2.2. Experimental Testbed

As shown in Figure 1, the experimental testbed for the DED and mechanical machining processes was constructed by retrofitting a four-axis CNC machine tool (DH-400-2Z, Harim Machinery, Anyang, Korea). A single-mode fiber laser (RFL-C750, Wuhan Raycus Fiber Laser Technologies) was connected to the DED head attached on the z-axis of the CNC machine tool in this testbed. The laser beam's diameter and wavelength were 3 mm and 1080 nm, respectively, and the distance between the DED head and substrate was set to 10 mm. In addition, the powders were supplied through a powder feeder (GTV Powder Feeder RF, GTV, Luckenbach, Germany) that was installed coaxially with the DED head, and argon was chosen as the delivering and shielding gas to supply metal powder to a melt pool and prevent oxidation of the DED parts during the process. During the process, a laser chiller (YRC-2000, Yescool, Bucheon, Korea) cools the DED head to continuously maintain the inner temperature to prevent fault occurrence and unbalanced deposition layer formation due to overheating. Lastly, the high-frequency spindle installed on the w-axis can perform the mechanical machining of the DED parts.

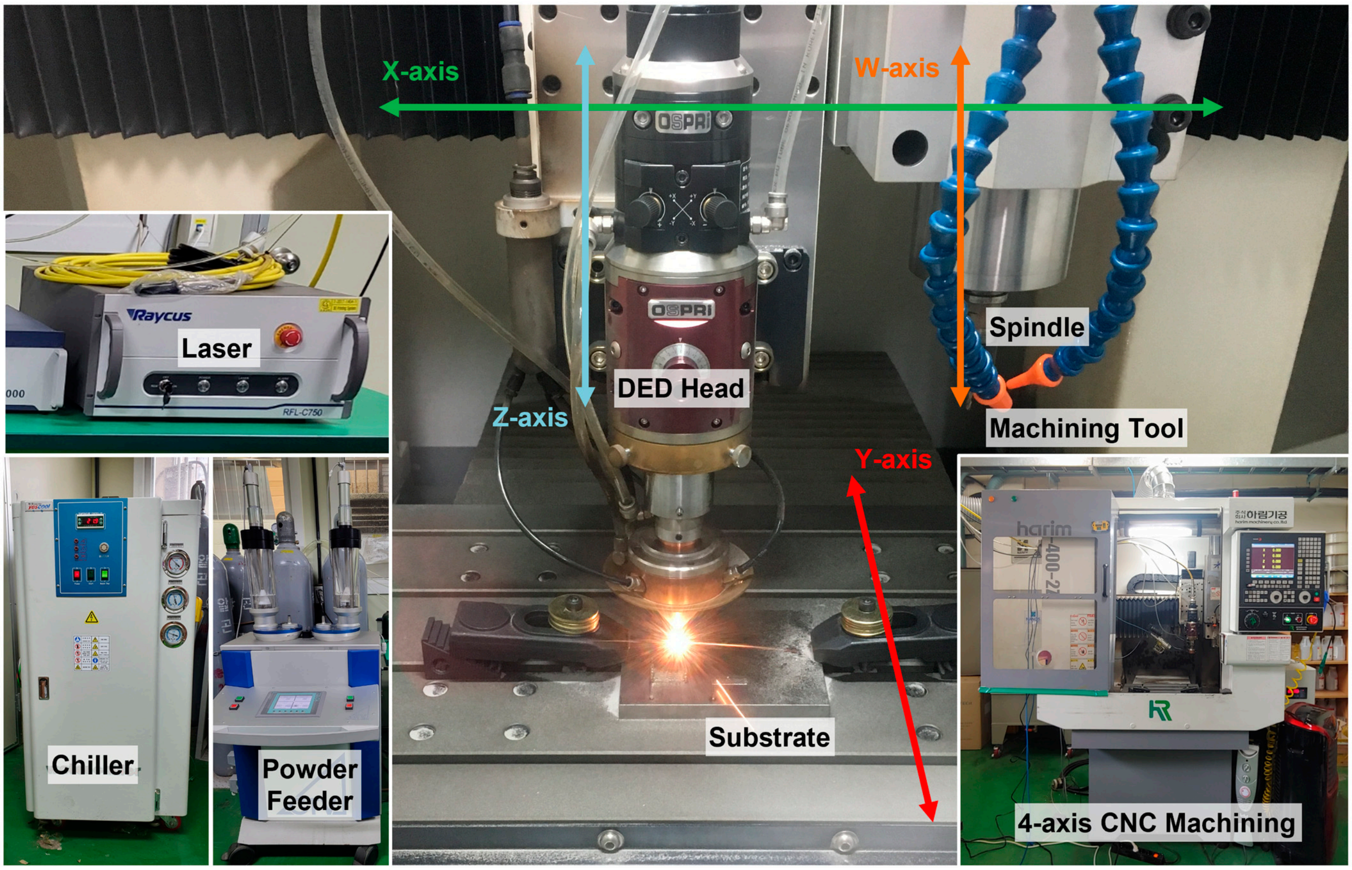

Figure 1. Experimental testbed for DED and machining processes.

2.3. Experimental Design and Conditions

As mentioned previously, two metallic powders, SAE 316L and Inconel 718, were deposited to produce a 6-layer FGM part with a graded structure using the DED process. For each layer, the weight composition ratios of SAE 316L and Inconel 718 were changed by 20 wt.%, from 0 wt.% to 100 wt.%, to produce the FGM part. Figure 2a is a schematic diagram of the FGM component with the composition ratios that change progressively for each layer.

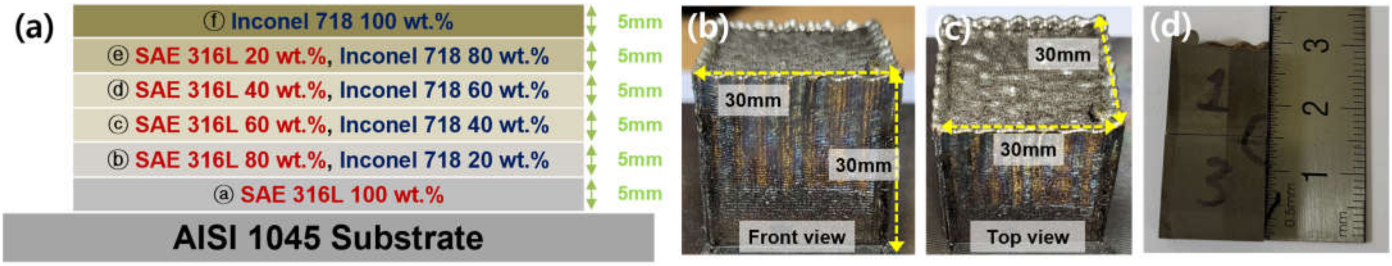

Figure 2. (**a**) Schematic diagram of the compositional ratios of each layer of the FGM and photos of (**b**) the deposited FGM in front view, (**c**) top view, and (**d**) the SEM/EDS analysis specimen.

Following a series of preliminary tests with extensive FGM fabrication and a defect analysis of specimens, it was determined that 300 W for laser power and 465 mm/min for scanning speed were the optimal DED process parameters without any defects. As a stacking technique, an orthogonal zigzag toolpath was employed to slightly enlarge each layer to compensate for excessive stacking during acceleration and deceleration sections. The DED experimental conditions are summarized in Table 2, and Figure 2b,c show photos of the deposited FGM part. The total height of the FGM part was designed to be 30 mm, and the height of each layer was 5 mm. After the FGM part fabrication, the part was sectioned using wire electrical discharge machining (EDM) for analysis. The sectioned specimen for the analysis can be seen in Figure 2d.

Table 2. The experimental conditions of DED process for FGM part fabrication.

Composition Percentage (wt.%)	Laser Power (W)	Scanning Speed (mm/min)	Mass Flow Rate of Powder (g/min)	Flow Rate of Delivery Gas (L/min)	Flow Rate of Shielding Gas (L/min)	DED Head Distance to Substrate (mm)	Overlap (%)
20	300	465	10	14	14	10	31

3. Metallographic Characteristics

3.1. Compositions

In order to verify the compositional variations in the FGM part, 5 × 5 mm specimens were cut from each of the six layers using wire EDM. An energy-dispersive X-ray spectroscopy (EDS) analysis was then performed on each specimen at three specific depths of 1 mm, 2.5 mm, and 4 mm, using a scanning electron microscope (SEM) apparatus (SNE-4500M, SEC, Suwon, Korea), and those SEM images with EDS results for these measurements can be seen in Figure 3. At each of these three depths, horizontal measurements were repeated three times, resulting in a total of nine analyses for each layer. The average values of these analyses are presented in Figure 4.

As shown in Figure 4, the FGM was fabricated through six layers, transitioning from 100 wt.% SAE 316L in Figure 4a to 100 wt.% Inconel 718 in Figure 4f. Specifically, Figure 4b shows a composition of 80 wt.% SAE 316L and 20 wt.% Inconel 718. With each successive layer, the composition of SAE 316L decreased by 20 wt.% while that of Inconel 718 increased by the same amount. Correspondingly, the Fe content progressively diminished from the initial value of 60 wt.% in the SAE 316L 100 wt.% layer to 17–18 wt.% in the Inconel 718 100 wt.% layer, which can be confirmed by the typical Inconel 718 Fe ratio in Table 1. Conversely, the Ni composition rises, starting from the 12 wt.% inherent in SAE 316L and incrementally increasing with the enhanced content of Inconel 718. These compositional shifts can be clearly observed in Figure 4. The niobium equivalent, which has a big impact on the formation of the secondary phase in Inconel 718, was also seen to gradually rise as the composition ratio of Inconel 718 rose. Thus, the composition analysis confirmed that the FGM part was properly deposited, as were the ratios of the metal elements in the layered structure.

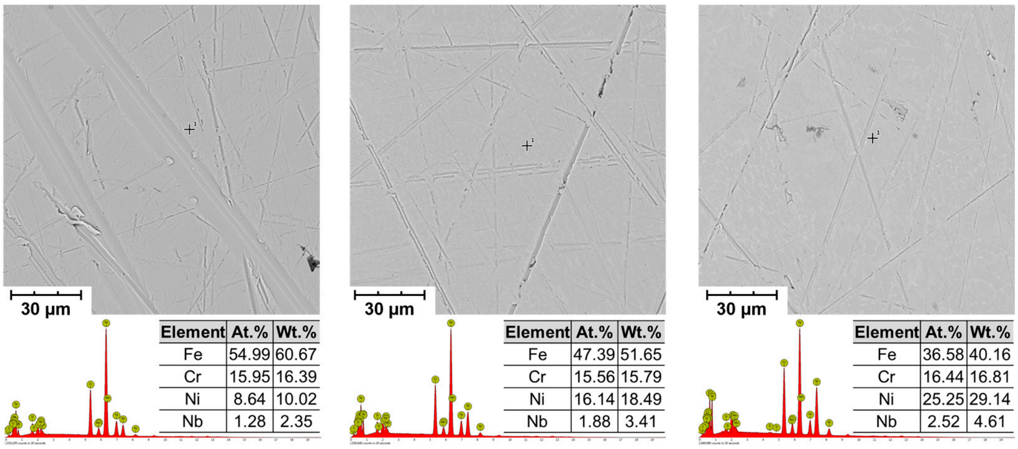

Element	At.%	Wt.%
Fe	54.99	60.67
Cr	15.95	16.39
Ni	8.64	10.02
Nb	1.28	2.35

(a) SAE 316L 100 wt.%

Element	At.%	Wt.%
Fe	47.39	51.65
Cr	15.56	15.79
Ni	16.14	18.49
Nb	1.88	3.41

(b) SAE 316L 80 wt.%, Inconel 718 20 wt.%

Element	At.%	Wt.%
Fe	36.58	40.16
Cr	16.44	16.81
Ni	25.25	29.14
Nb	2.52	4.61

(c) SAE 316L 60 wt.%, Inconel 718 40 wt.%

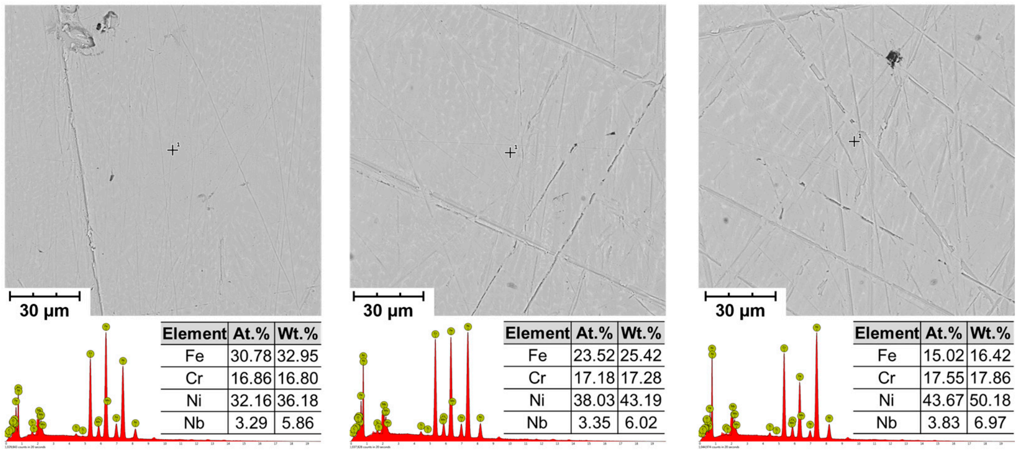

Element	At.%	Wt.%
Fe	30.78	32.95
Cr	16.86	16.80
Ni	32.16	36.18
Nb	3.29	5.86

(d) SAE 316L 40 wt.%, Inconel 718 60 wt.%

Element	At.%	Wt.%
Fe	23.52	25.42
Cr	17.18	17.28
Ni	38.03	43.19
Nb	3.35	6.02

(e) SAE 316L 20 wt.%, Inconel 718 80 wt.%

Element	At.%	Wt.%
Fe	15.02	16.42
Cr	17.55	17.86
Ni	43.67	50.18
Nb	3.83	6.97

(f) Inconel 718 100 wt.%

Figure 3. SEM images and EDS analysis results for each layer of FGM.

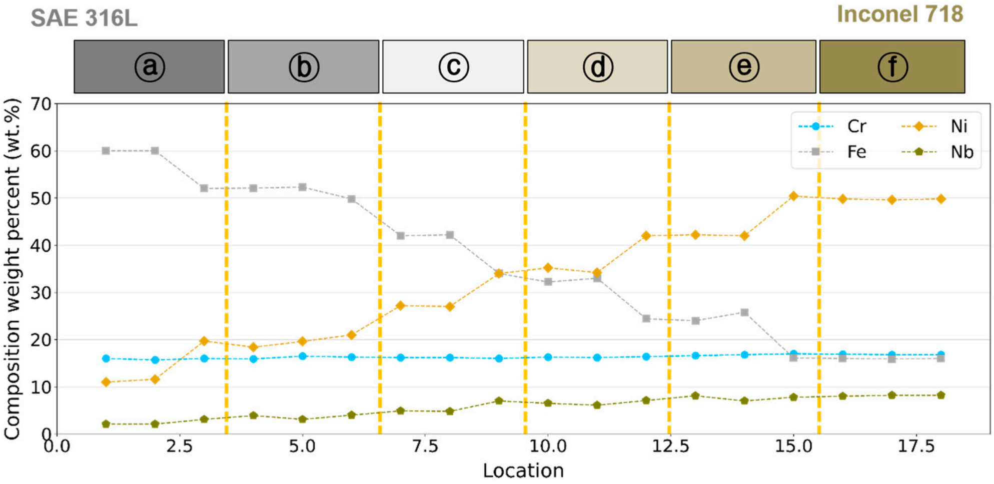

Figure 4. Measured composition ratios for each layer of the FGM part based on the EDS analysis.

3.2. Microstructure

The microstructure of the FGM part was investigated through a metallographic analysis using a microscope. To prepare for the microscope examination, the FGM specimens were sectioned layer by layer using wire EDM. The cut surfaces were then polished and subjected to etching. The appropriate etching times varied for each layer: 8 min for SAE

316L 100 wt.%, 16 min for Inconel 718 100 wt.%, and an additional 2 min of etching time for every 20 wt.% increase in Inconel 718 content. Following the ASTM E407 standard, 100× magnification images of each layer were captured using the microscope, and these images are presented in Figure 5.

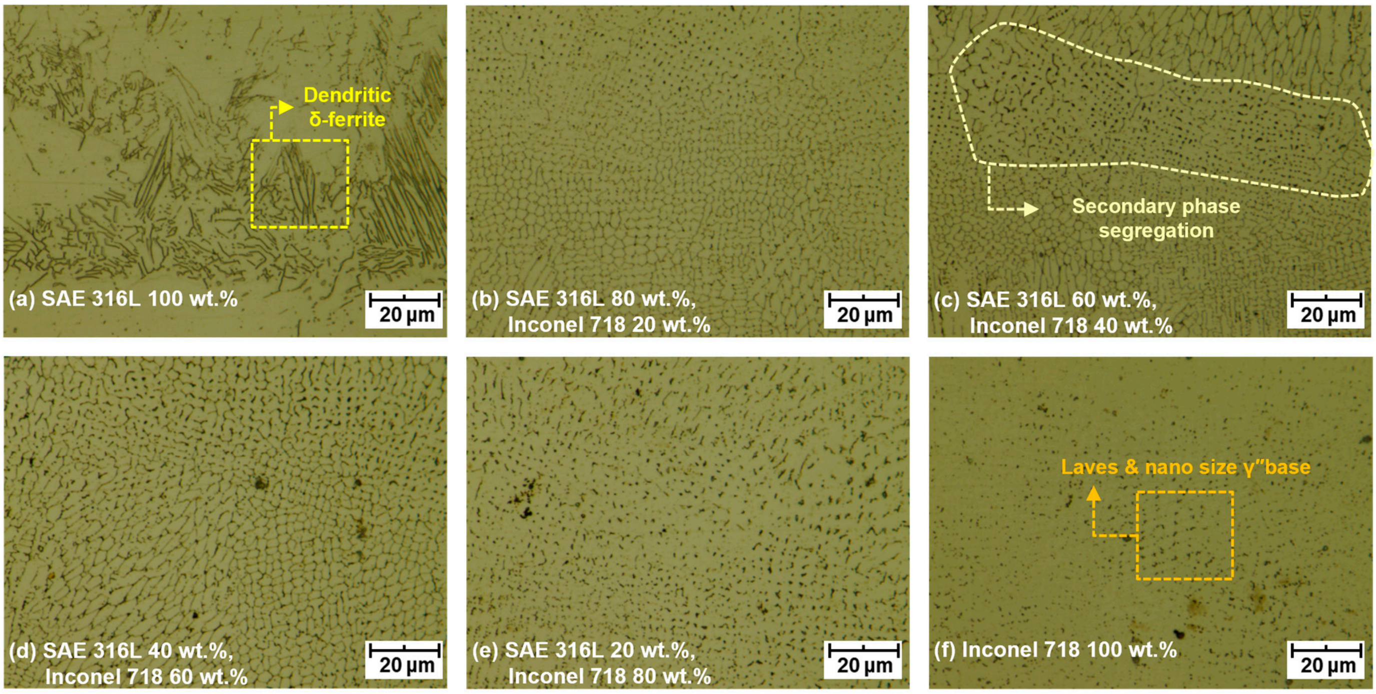

Figure 5. The microscopic images of each layer of the FGM part.

For the layer of 100 wt.% of SAE 316L, δ-ferrite dendritic structures can be observed, as shown in Figure 5a, which may be a result of rapid cooling during the DED process. In addition, as seen in Figure 5b, which shows the layer of 80 wt.% for SAE 316L and 20 wt.% for Inconel 718, the addition of Inconel 718 results in the formation of equiaxed grains and the complete disappearance of ferrite dendritic structures. This may be due to the slower cooling rate caused by the residual heat in the layer that was previously deposited.

Additionally, equiaxed austenite grain structures are preserved when the Inconel 718 component ratio is between 40 and 60 wt.%. However, the boundaries of austenitic grains begin to disintegrate when the Inconel 718 component ratio reaches 80 wt.%. At a 100 wt.% Inconel 718 component ratio, only irregularly shaped Laves phase precipitates are observed, as illustrated in Figure 5e,f. This phenomenon is likely attributable to the increasing levels of nickel and niobium equivalents as the Inconel 718 component ratio rises. As indicated by the EDS analysis results presented previously in Figure 4, the increase in nickel and niobium equivalents leads to the precipitation of the γ'' (NiNb) secondary phase within the pre-existing austenitic grains, thereby disrupting the austenitic grain boundaries [33].

To explain the experimental results empirically, the Schaeffler diagram was selected. The Schaeffler diagram is well-known for its ability to predict phase transitions in weld metal microstructures using the nickel and chromium equivalents of ferrous alloys [34]. It serves as a tool for anticipating or comparing the microstructure of molten alloys and stainless steel. Equations (1) and (2) outline the procedures for calculating the chromium and nickel equivalents needed for the analysis using the Schaeffler diagram.

$$\text{Chromium equivalent} = \%\text{Cr} + 1.5\%\text{Si} + 0.5\%\text{Nb (wt.\%)} \tag{1}$$

$$\text{Nickel equivalent} = \%\text{Ni} + 30\%\text{C} + 0.5\%\text{Mn (wt.\%)} \tag{2}$$

The positions of each layer in the FGM parts on the Schaeffler diagram, based on varying composition ratios, can be confirmed in Figure 6 using the calculations from Equations (1) and (2). The data predict a complete austenite phase for areas with an Inconel 718 composition ratio of 20 wt.% or higher [35]. This aligns with the earlier metallographic microscope observations in Figure 5, which showed the formation of δ-ferrite structures with dendritic phases in the areas with a SAE 316L 100 wt.% composition. Additionally, as the Inconel 718 component ratio increases, these δ-ferrite structures with dendritic phases disappear, giving way to newly formed equiaxed austenite grain structures. This transition is attributed to both a slower cooling rate and an increase in the Inconel 718 component ratio, and it was confirmed that the results of the Schaeffler diagram predictions align with the actual measured microstructures in Figure 5.

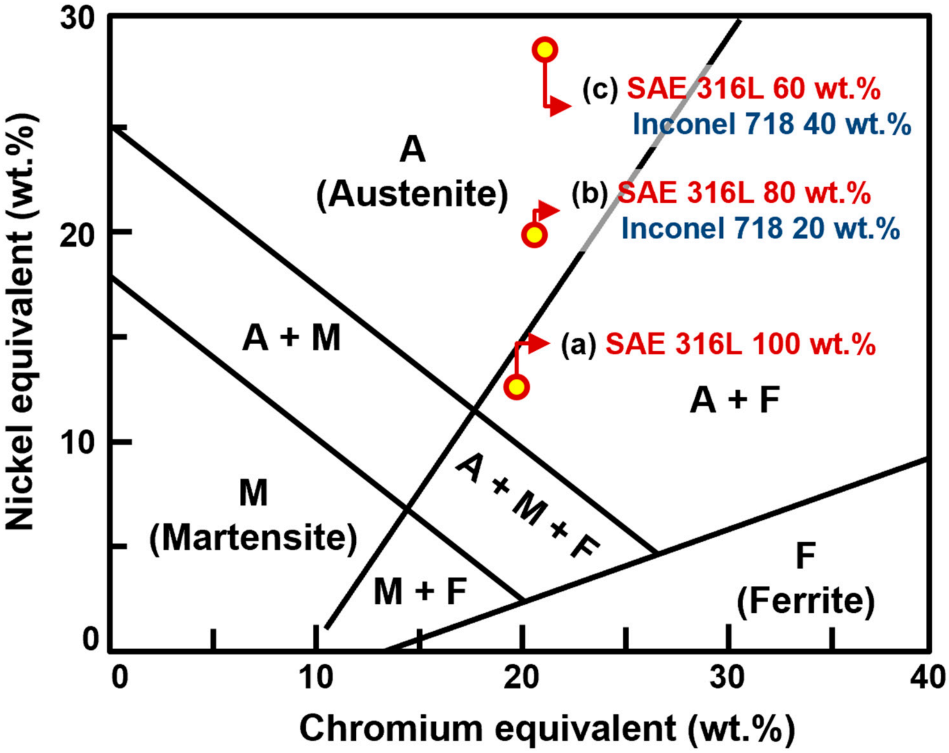

Figure 6. Schaeffler diagram for the FGM part.

An X-ray diffraction (XRD, Empyrean, Malvern Panalytical, Malvern, UK) analysis was also performed. The XRD results for all six layers of the FGM part can be seen in Figure 7. Prior to analyzing the FGM via XRD, it is essential to understand the characteristic XRD profiles of typical SAE 316L and Inconel 718. In the case of 100 wt.% SAE 316L, an austenitic stainless steel, a notable peak is observed that corresponds to the austenite phase. This peak arises due to the stabilizing influence of nickel, an element that allows the material to maintain an austenitic structure with carbon dissolved in the face-centered cubic (FCC) γ-Fe structure. A body-centered cubic (BCC) δ-ferrite structure is also present at room temperature [36]. Similarly, Inconel 718 features secondary phases such as γ' (Ni[Al,Ti]), γ'' (NiNb), and δ (NiNb) on the basis of its nickel-based FCC austenite (γ) structure. Among these, the γ'' phase serves as the primary strengthening phase to improve the strength of the material, whereas the γ' phase acts as a secondary strengthening phase, and the δ phase is precipitated along the grain boundary from the γ'' phase. Notably, rapid cooling of molten Inconel 718 can lead to the precipitation of the Laves phase (NiNb, FeNb), which is characterized by high hardness and can cause cracks in the alloy [37].

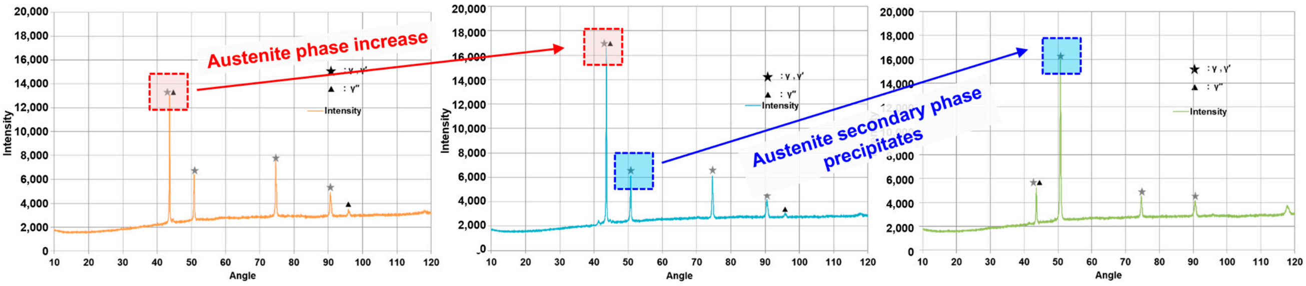

(a) SAE 316L 100 wt.% (b) SAE 316L 80 wt.%, Inconel 718 20 wt.% (c) SAE 316L 60 wt.%, Inconel 718 40 wt.%

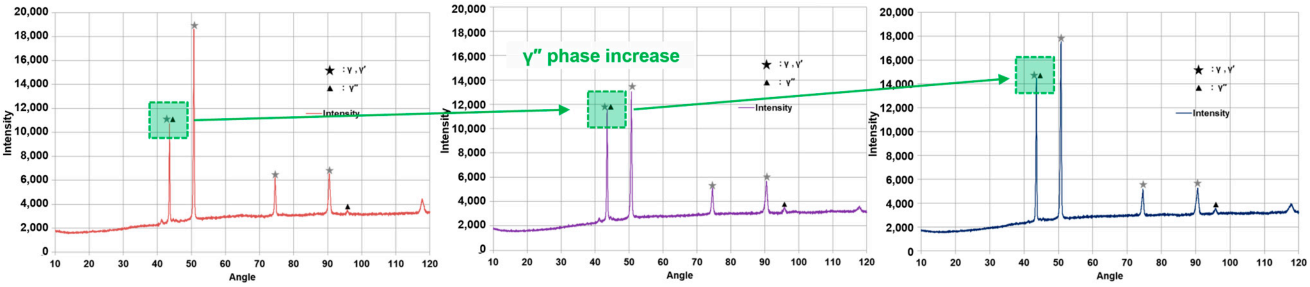

(d) SAE 316L 40 wt.%, Inconel 718 60 wt.% (e) SAE 316L 20 wt.%, Inconel 718 80 wt.% (f) Inconel 718 100 wt.%

Figure 7. XRD analysis results of the FGM part.

Based on the characteristic XRD profiles of typical SAE 316L and Inconel 718, the correlation between the previously analyzed microstructure, Schaeffler diagram results of the FGM part, and measured XRD results were examined. As shown in Figure 7, the analysis results can be categorized into two groups. The first group includes SAE 316L 100 wt.% and SAE 316L 80 wt.% mixed with Inconel 718 20 wt.% and shown in Figure 7a,b. The second group comprises the remaining composition ratio area.

In the first group, the XRD spectrum of the SAE 316L 80 wt.% mixed with Inconel 718 20 wt.% area exhibited a peak intensity around 40 degrees that was 28.57% higher compared to SAE 316L 100 wt.%. This peak was attributed to the austenite microstructure, corroborating both the microstructural analysis in Figure 5a,b and Schaeffler diagram in Figure 6 that indicate a fully austenitic phase in the SAE 316L 80 wt.% mixed with Inconel 718 20 wt.% region.

On the other hand, the XRD spectrum of the SAE 316L 60 wt.% mixed with Inconel 718 40 wt.% area revealed a rapid decline in the peak intensity around 40 degrees and an increase in intensity around 50 degrees. This change is ascribed to the formation of the γ' (Ni[Al,Ti]) phase, one of the austenitic secondary phases. It suggests that increasing nickel content induces the appearance of additional secondary phases alongside the existing complete austenite phase, as evidenced in Figure 5c.

Finally, although the peak intensity around 40 degrees initially decreased sharply, it gradually increased again up to Inconel 718 100 wt.%, resulting in a 159.65% increase compared to the region with Inconel 718 40 wt.%, as can be seen in Figure 7d–f. This resurgence in intensity is interpreted as the γ'' phase also contributing to this peak. Thus, the elevated peak intensity corresponds to the microstructural analysis showing that higher Inconel 718 content leads to excessive precipitation of the γ'' phase, resulting in the dissolution of the austenite grains.

3.3. Mechanical Properties

After the microstructure analysis of the FGM part, a mechanical property analysis was carried out for each region and transitional boundary of the gradual variation area. Hardness measurements were taken at 1 mm intervals, ranging from the SAE 316L 100 wt.% area to the Inconel 718 100 wt.% area on the opposite side of the deposited FGM specimen that was cut for the microstructure analysis as shown in Figure 2d. Micro-Vickers hardness tests were performed in accordance with ASTM E384 standards. To ensure reliability, each measurement was repeated four times using a 100 g load and a 10 s holding time. The average values are presented in Figure 8.

As shown in Figure 8a,b, a slight decrease in hardness was observed, where SAE 316L 100 wt.% changed to SAE 316L 80 wt.% mixed with Inconel 718 20 wt.%. This drop in hardness is related to the microstructural change from a high-hardness dendritic δ-ferrite structure to an equiaxed austenite grain, as shown in Figure 5a,b. Additionally, while forming a refined microstructure, the secondary phase segregation observable in Figure 5c enhances the material's strength at grain boundaries. Thus, the measured hardness increased in the case of SAE 316L 60 wt.% and Inconel 718 40 wt.% in general, as shown in Figure 8c. However, in some areas, it precipitates excessively, weakening the boundaries. Such results can be correlated with the significant hardness fluctuation seen in Figure 8c for that layer. In addition, as seen in Figure 8d–f, the hardness values appeared to stabilize, showing only a minor fluctuation trend in the cases of higher Inconel 718 (60, 80, and 100 wt%) compositions. These stable hardness values can be related to the constant niobium (Nb) equivalent values, as depicted in Figure 4, which significantly influence the precipitation of the Laves phase.

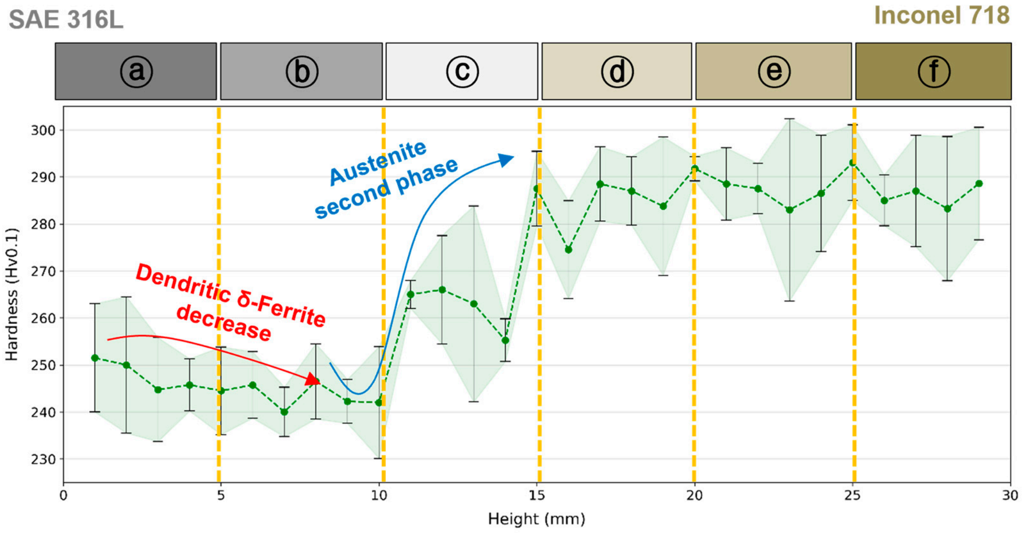

Figure 8. Measured microhardness results of the FGM part.

4. Machining Characteristics

4.1. Milling Experiments

A series of milling experiments for the FGM parts were conducted using the machining spindle of the experimental testbed given in Figure 1. To investigate the machining characteristics of the FGM part, the milling method and path were considered. For the milling method, both upward and downward milling processes were considered, as well as the cutting direction from SAE 316L to Inconel 718, and vice versa, for the milling path.

To ensure the reliability of the experiments, 60 passes were conducted twice under identical conditions for each test case. Two FGM specimens were prepared using wire EDM to smooth the surface and remove the oxide layers. A 2-flute end mill with a 6 mm diameter (2HCEG060150S06, Jjtools, Seoul, Korea) was used for the milling processes. Each specimen underwent 15 passes along a 30 mm milling path, featuring an axial depth of cut at 0.3 mm and a radial depth of cut at 0.6 mm, making for a total cut length of 450 mm.

The experimental conditions are summarized in Table 3, and four experimental cases were sorted out, as can be seen in Table 4. In addition, the schematic diagram illustrating the milling methods and paths is given in Figure 9a, and the photos of the milled surfaces of four experimental cases are shown in Figure 9b.

Table 3. Experimental conditions for the milling processes.

Spindle Speed [1] (RPM)	Feed Rate [2] (mm/min)	Feed per Tooth [3] (mm/Tooth)
5305	955	0.09

[1] Measured machine tool's spindle rotational speed, [2] Speed at which a tool progresses during machining, [3] Distance a tool advances for each rotation of a cutting tooth during machining.

Table 4. Experimental cases for the milling processes.

Case	Milling Method	Milling Path
Case 1	Downward milling	SAE 316L → Inconel 718
Case 2	Downward milling	Inconel 718 → SAE 316L
Case 3	Upward milling	SAE 316L → Inconel 718
Case 4	Upward milling	Inconel 718 → SAE 316L

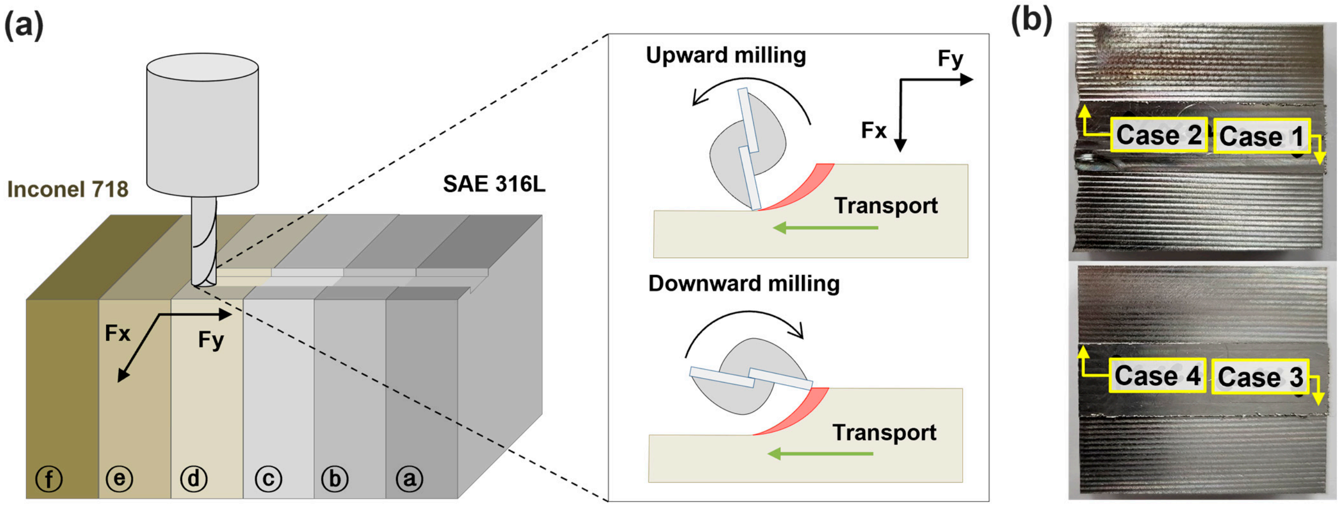

Figure 9. (**a**) Schematic diagram of the FGM machining process for milling methods and paths. (**b**) Photos of the milled surfaces of each experimental case.

Moreover, a signal acquisition system was configured to collect cutting force during the FGM milling process. A tool dynamometer (9257B, Kistler, Winterthur, Switzerland) and a signal amplifier (5167A81DK, Kistler, Winterthur, Switzerland) were used for milling force measurement, with calibration conducted using weights before data acquisition. The data were collected at a sampling rate of 2500 Hz during the first 15 passes of 60 passes, and approximately 4700 sampled values were collected for each milling pass. To analyze the variations in the milling force according to the changes in the material's characteristics and properties, the entire milling force signal of each pass in x-direction and y-direction, as depicted in Figure 9, was divided into 335 regions based on 14 signals collected per tool rotation for downsampling. The overall milling force signal was calculated by Equation (3) of 14 values, and the milling force signals are depicted in Figure 10. By using the overall milling force signals, both the average milling force for the entire process and the average milling force for each pass were calculated to provide insights into the FGM machining process.

$$F = \sqrt{F_x^2 + F_y^2} \tag{3}$$

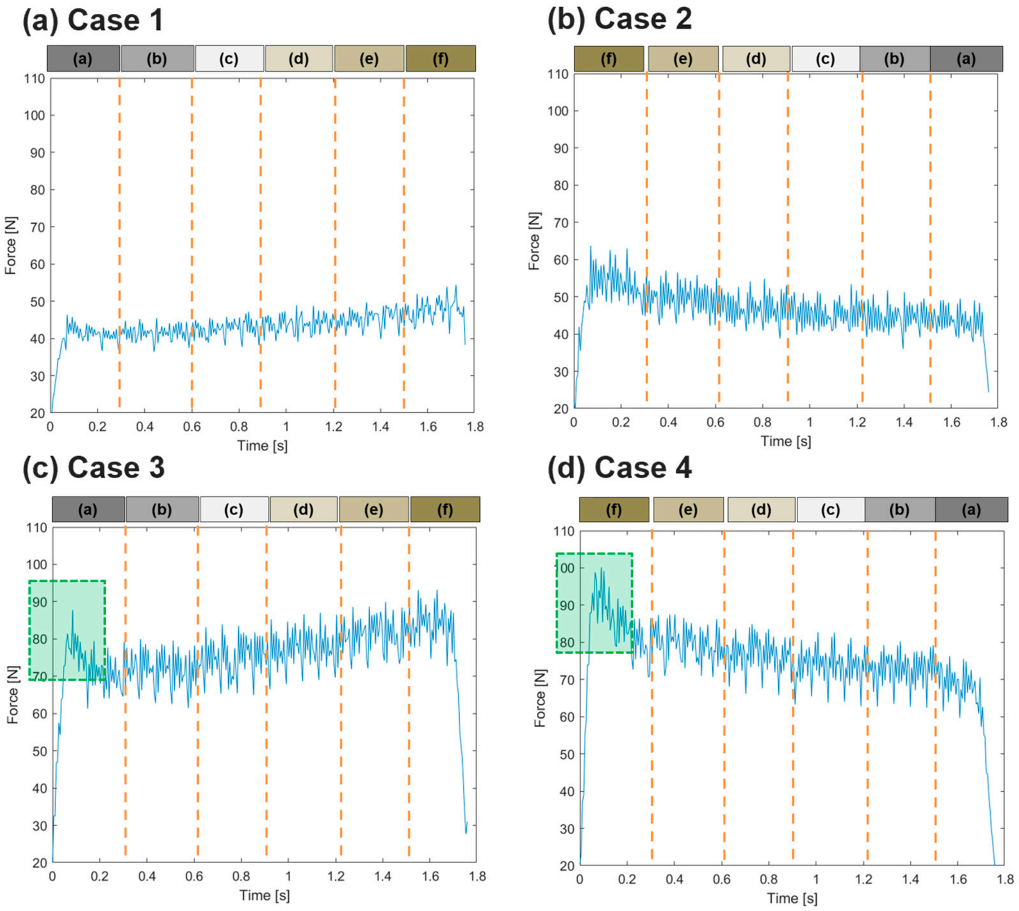

Figure 10. The measured milling force signals of each experimental case during 1-pass milling.

4.2. Cutting Force

The analysis of the measured milling force revealed a trend that aligns with changes in material properties during the milling process, as illustrated in Figure 10. Specifically, in cases 2 and 4—where the milling direction was from the relatively high-hardness Inconel 718 towards SAE 316L—the milling force decreased as the process advanced. Conversely, in cases 1 and 3, a gradual increase in milling force was observed. Additionally, the milling force signals obtained through upward milling displayed a pronounced peak in the entry region, as can be seen in Figure 10c,d. This phenomenon was attributed to the coinciding directions of tool feed and milling rotation, which resulted in a significant impact force during the initial phase.

In addition, the average milling force was calculated over a total of 15 repeated milling passes for each case twice, as depicted in Figure 11. This revealed significant differences in both milling methods and milling paths, and it was observed that upward milling generated greater force than downward milling. The consistency between two repeated trials in each experimental case validates the reproducibility of the results.

To delve deeper into the variations in the milling force, data were collected for each of the 15 milling passes, as displayed in Figure 12. In the case of upward milling from SAE 316L to Inconel 718, as the number of milling cycles increased, so did the milling force. However, when milling from Inconel 718 to SAE 316L, relatively constant milling forces were observed. In the case of downward milling, neither the milling path nor the number of milling paths had a significant effect, indicating a stable milling process by maintaining a relatively constant milling force throughout the process.

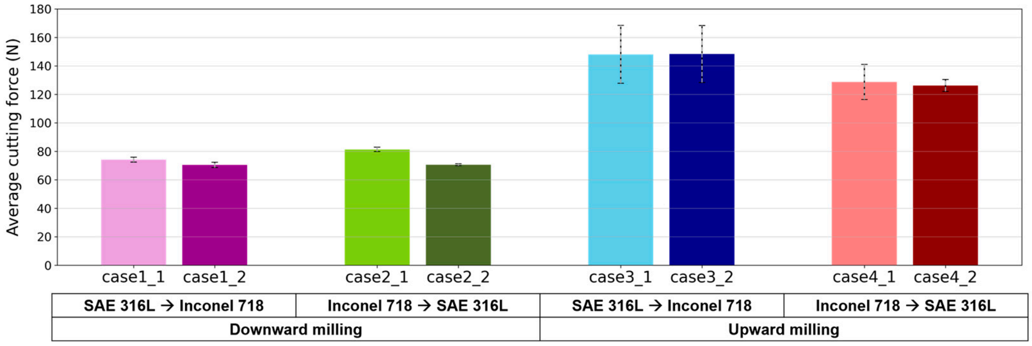

Figure 11. The average milling forces of 15 passes for each experimental case.

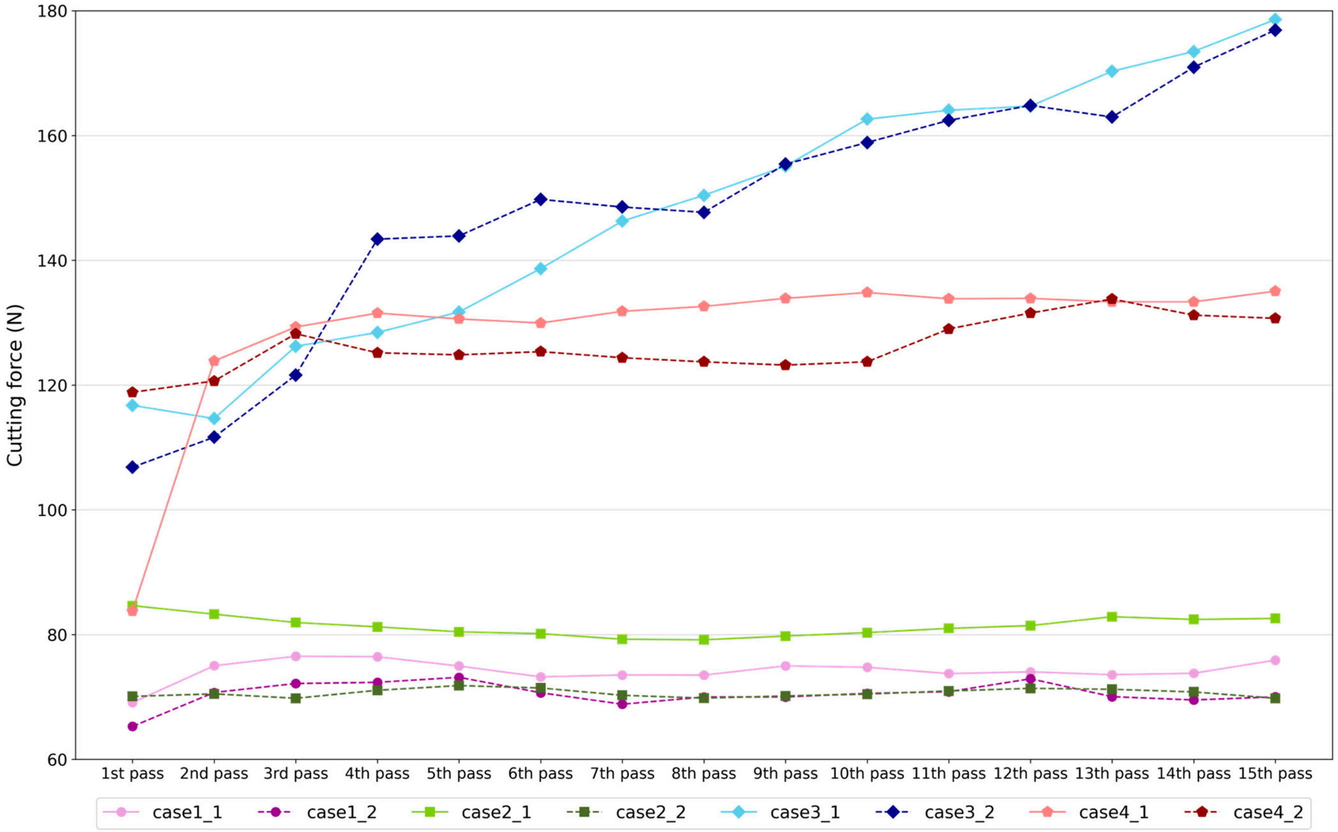

Figure 12. The milling forces according to individual passes for each experimental case.

4.3. Tool Wear

During the FGM milling process, the tool wear pattern that occurs as the milling process progresses can be observed in Figure 13a, and the quantified results of tool wear can also be found in Figure 13b. Tool wear is generally more severe in upward milling than in downward milling, and these results are consistent with the milling force measurement results in Figure 11, showing a significant difference between upward milling and downward milling methods.

As shown in Figure 13a, the most severe tool wear was observed in case 3 when the upward milling process progressed from SAE 316L to Inconel 718. In this case, as shown in Figure 12, the milling force increased considerably as the number of passes increased, and tool fracture occurred after 60 milling passes, as shown in Figure 13b.

A comparative analysis of the FGM milling experiment results indicates significant variances in machinability depending on the milling path during the upward FGM milling process. The difference in milling mechanism arises from the variations in material strength, which manifest during upward milling of the FGM. Specifically, the impact force is applied differently to SAE 316L 100 wt.% and Inconel 718 100 wt.% areas, depending on the milling path chosen. Starting the milling process in the SAE 316L area can result in tool damage due to strong impact forces, leading to a considerable increase in milling force as a consequence of tool wear, as depicted in Figure 13a case 3. On the other hand, starting in the Inconel 718 area, which has gummy behavior and leads to adhesive wear, presents a different challenge: irregular Laves phases, as depicted in Figure 5f, can precipitate within the material, resulting in cracks and reduced impact strength, thereby leading to material fragmentation. As a consequence, despite the higher microhardness of Inconel 718 compared to SAE 316L, tool damage occurs less frequently when milling starts in the Inconel 718 area. This reduced tool damage, as can be observed in Figure 12, ensures that even with repeated milling processes, a consistent cutting force is maintained when starting from the Inconel 718 area compared to when starting from the SAE 316L area.

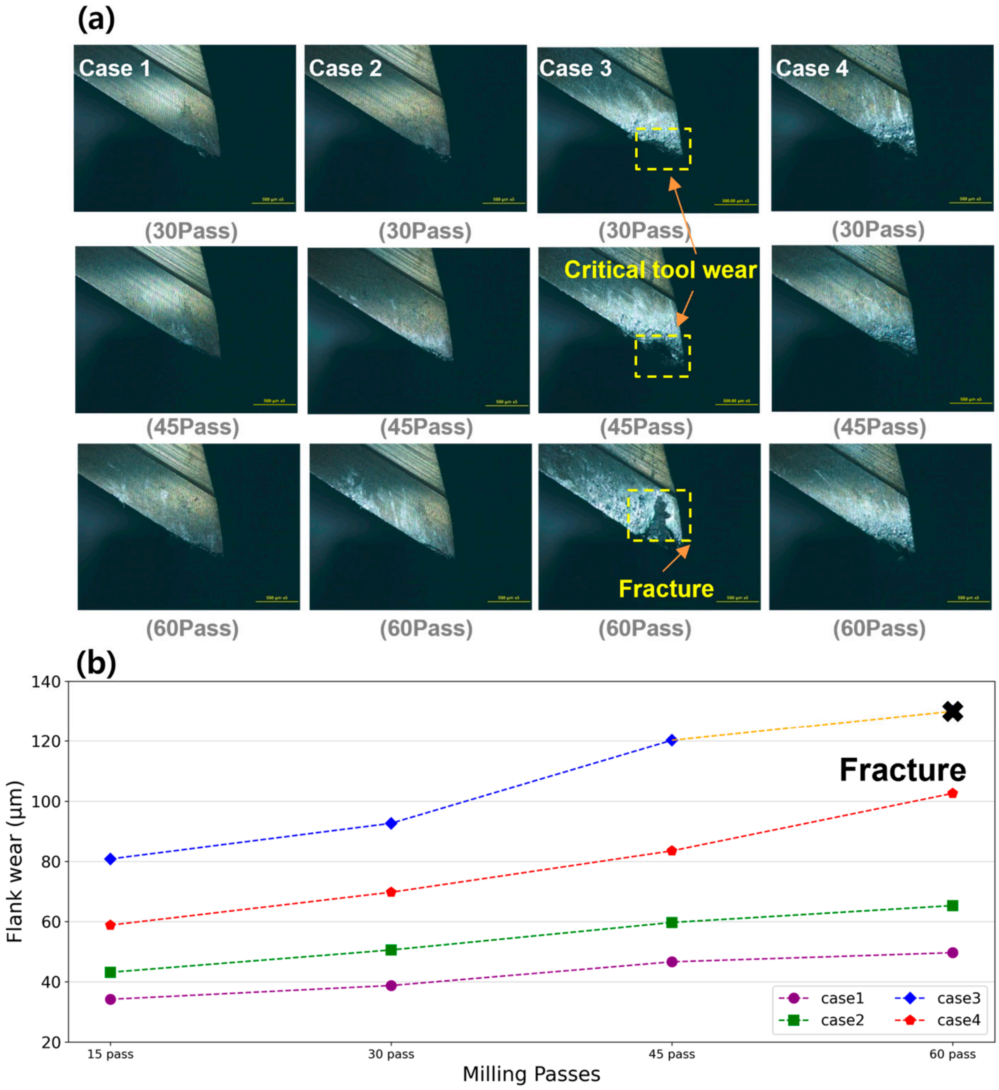

Figure 13. (**a**) Tool images after 30 passes for each case. (**b**) Comparative analysis of quantified flank wear values.

5. Conclusions

In this study, an FGM composed of SAE 316L and Inconel 718 was fabricated using the DED process. This process, which employs a high-energy heat source and metal melting, fabricates parts with high density and strength. After fabrication, the FGM specimens were subjected to microstructural and mechanical property analyses. Subsequently, machining characteristics, such as tool wear and milling force, were examined during the milling process of the FGM.

The microstructure and mechanical properties of the FGM consisting of SAE 316L and Inconel 718 were studied using metallographic microscopy, SEM/EDS and XRD analyses, complemented by microhardness measurements. The SEM/EDS analysis, conducted from the SAE 316L deposited region to the Inconel 718 region, showed a gradual increase in the Ni component from an initial 11.0 wt.% to 49.8 wt.%. Additionally, Nb, a significant influence component of secondary phase formation in the Inconel 718 alloy, also exhibited an increase of about 4 times in the 100 wt.% Inconel 718 region compared to its initial content. These observations confirm that the FGM was successfully deposited using the two materials. Furthermore, the microstructure and XRD results indicated a phase transition in the microstructure with changing material composition. Specifically, the δ-ferrite dendritic structure seen in pure SAE 316L disappeared, being replaced by a complete austenite phase as Inconel 718 was added. With increasing Inconel content, the austenite grains started disintegrating due to the secondary phase growth, revealing a microstructure dominated by Laves and γ'' phases. These observations were consistent with the microhardness values, which transitioned from an initial 250 Hv to 290 Hv, a 16% increase in hardness.

The optimal milling strategy for the FGM of SAE 316L and Inconel 718 was determined to be downward milling from SAE 316L towards Inconel 718. This decision was based on a minimum average cutting force of 72.335 N (48.8% of the maximum cutting force value) and an average wear distance of 42.320 μm during 60 milling passes. This post-processing strategy ensures the deposited FGM's suitability for high-temperature environments, such as turbine blades and combustion chambers in the aerospace industry, and for pipelines in the chemical and petroleum refining industries that operate under high temperatures and corrosive conditions.

Author Contributions: Conceptualization, I.N., J.J. and S.W.L.; methodology, I.N. and J.J.; software, I.N.; validation, I.N. and J.J.; formal analysis, I.N. and J.J.; investigation, J.J.; data curation, I.N. and J.J.; writing—original draft preparation, I.N.; writing—review and editing, S.W.L.; visualization, I.N.; supervision, S.W.L.; project administration, S.W.L.; funding acquisition, S.W.L. All authors have read and agreed to the published version of the manuscript.

Funding: This research was funded by the National Research Foundation of Korea (NRF)'s grant funded by the Korea Government (MSIT) (NRF-2018R1A2A1A05079477, NRF-2022R1A2C3012900).

Data Availability Statement: The data used in this research are available upon request from the corresponding author.

Conflicts of Interest: The authors declare no conflict of interest.

References

1. Guo, N.; Leu, M.C. Additive manufacturing: Technology, applications and research needs. *Front. Mech. Eng.* **2013**, *8*, 215–243. [CrossRef]
2. Wong, K.V.; Hernandez, A. A review of additive manufacturing. *Int. Sch. Res. Not.* **2012**, *2012*, 1–10. [CrossRef]
3. Frazier, W.E. Metal additive manufacturing: A review. *J. Mater. Eng. Perform.* **2014**, *23*, 1917–1928. [CrossRef]
4. Mellor, S.; Hao, L.; Zhang, D. Additive manufacturing: A framework for implementation. *Int. J. Prod. Econ.* **2014**, *149*, 194–201. [CrossRef]
5. Dilberoglu, U.M.; Gharehpapagh, B.; Yaman, U.; Dolen, M. The role of additive manufacturing in the era of industry 4.0. *Procedia Manuf.* **2017**, *11*, 545–554. [CrossRef]
6. Ahn, D.G. Direct metal additive manufacturing processes and their sustainable applications for green technology: A review. *Int. J. Precis. Eng. Manuf. Green Technol.* **2016**, *3*, 381–395. [CrossRef]
7. Kim, J.S.; Kang, B.J.; Lee, S.W. An experimental study on microstructural characteristics and mechanical properties of stainless-steel 316L parts using directed energy deposition (DED) process. *J. Mech. Sci. Technol.* **2019**, *33*, 5731–5737. [CrossRef]
8. Duda, T.; Raghavan, L.V. 3D metal printing technology. *IFAC Pap.* **2016**, *49*, 103–110. [CrossRef]
9. Saboori, A.; Aversa, A.; Marchese, G.; Biamino, S.; Lombardi, M.; Fino, P. Application of directed energy deposition-based additive manufacturing in repair. *Appl. Sci.* **2019**, *9*, 3316. [CrossRef]

10. Loh, G.H.; Pei, E.; Harrison, D.; Monzón, M.D. An overview of functionally graded additive manufacturing. *Addit. Manuf.* **2018**, *23*, 34–44. [CrossRef]
11. Zhao, K.; Zhang, G.; Ma, G.; Shen, C.; Wu, D. Microstructure and mechanical properties of titanium alloy/zirconia functionally graded materials prepared by laser additive manufacturing. *J. Manuf. Process.* **2020**, *56*, 616–622. [CrossRef]
12. Geng, Y.; Xie, W.; Tu, Y.; Deng, S.; Egan, D.; Dowling, D.P.; Song, H.; Zhang, S.; Harrison, N. Ti–6Al–4V microstructural functionally graded material by additive manufacturing: Experiment and computational modelling. *Mater. Sci. Eng. A* **2021**, *823*, 141782. [CrossRef]
13. Rani, K.U.; Kumar, R.; Mahapatra, M.M.; Mulik, R.S.; Świerczyńska, A.; Fydrych, D.; Pandey, C. Wire arc additive manufactured mild steel and austenitic stainless steel components: Microstructure, mechanical properties and residual stresses. *Materials* **2022**, *15*, 7094. [CrossRef] [PubMed]
14. Sanjeeviprakash, K.; Kannan, A.R.; Shanmugam, N.S. Additive manufacturing of metal-based functionally graded materials: Overview, recent advancements and challenges. *J. Braz. Soc. Mech. Sci. Eng.* **2023**, *45*, 241. [CrossRef]
15. Liverani, E.; Fortunato, A. Additive manufacturing of AISI 420 stainless steel: Process validation, defect analysis and mechanical characterization in different process and post-process conditions. *Int. J. Adv. Manuf. Technol.* **2021**, *117*, 809–821. [CrossRef]
16. Fan, W.; Zhang, C.; Tan, H.; Wang, Y.; Peng, Y.; Zhang, F.; Lin, X.; Huang, W. Microstructures and mechanical properties of Invar/MnCu functionally graded material fabricated by directed energy deposition. *Mater. Sci. Eng. A* **2022**, *860*, 144332. [CrossRef]
17. Su, Y.; Chen, B.; Tan, C.; Song, X.; Feng, J. Influence of composition gradient variation on the microstructure and mechanical properties of 316 L/Inconel718 functionally graded material fabricated by laser additive manufacturing. *J. Mater. Process. Technol.* **2020**, *283*, 116702. [CrossRef]
18. Zhang, X.; Chen, Y.; Liou, F. Fabrication of SS316L-IN625 functionally graded materials by powder-fed directed energy deposition. *Sci. Technol. Weld. Join.* **2019**, *24*, 504–516. [CrossRef]
19. Rodrigues, T.A.; Farias, F.W.C.; Zhang, K.; Shamsolhodaei, A.; Shen, J.; Zhou, N.; Schell, N.; Capek, J.; Polatidis, E.; Santos, T.G.; et al. Wire and arc additive manufacturing of 316L stainless steel/Inconel 625 functionally graded material: Development and characterization. *J. Mater. Res. Technol.* **2022**, *21*, 237–251. [CrossRef]
20. Yu, X.; Xue, J.; Shen, Q.; Zheng, Z.; Ou, N.; Wu, W. Dual-wire plasma arc additively manufactured SS 316l-Inconel 625 functionally graded material: Microstructure Evolution and mechanical properties. *J. Mater. Eng. Perform.* **2023**, *32*, 1412–1422. [CrossRef]
21. Kim, S.H.; Lee, H.; Yeon, S.M.; Aranas, C., Jr.; Choi, K.; Yoon, J.; Yang, S.W.; Lee, H. Selective compositional range exclusion via directed energy deposition to produce a defect-free Inconel 718/SS 316L functionally graded material. *Addit. Manuf.* **2021**, *47*, 102288. [CrossRef]
22. Li, T.; Wang, Z.; Hu, S.; Yang, Z.; Wang, Y. Hot cracking during the fabrication of Inconel 625/stainless steel 308 L functionally graded material by dual-wire arc additive manufacturing. *J. Manuf. Process.* **2022**, *82*, 461–473. [CrossRef]
23. Yang, S.W.; Yoon, J.; Lee, H.; Shim, D.S. Defect of functionally graded material of inconel 718 and STS 316L fabricated by directed energy deposition and its effect on mechanical properties. *J. Mater. Res. Technol.* **2022**, *17*, 478–497. [CrossRef]
24. Carroll, B.E.; Otis, R.A.; Borgonia, J.P.; Suh, J.O.; Dillon, R.P.; Shapiro, A.A.; Hofmann, D.C.; Liu, Z.K.; Beese, A.M. Functionally graded material of 304L stainless steel and inconel 625 fabricated by directed energy deposition: Characterization and thermodynamic modeling. *Acta Mater.* **2016**, *108*, 46–54. [CrossRef]
25. Venkatachalam, A.; Anurag, P.V.S.; Sadanand, T.D.; Nachimuthu, R. Optimization of the milling parameters for an Al/Si3N4 functionally graded composite using grey relational analysis. *Mater. Test.* **2018**, *60*, 215–221. [CrossRef]
26. Liu, D.; Liu, Z.; Zhao, J.; Song, Q.; Ren, X.; Ma, H. Tool wear monitoring through online measured cutting force and cutting temperature during face milling Inconel 718. *Int. J. Adv. Manuf. Technol.* **2022**, *122*, 729–740. [CrossRef]
27. Martyushev, N.V.; Kozlov, V.N.; Qi, M.; Tynchenko, V.S.; Kononenko, R.V.; Konyukhov, V.Y.; Valuev, D.V. Production of Workpieces from Martensitic Stainless Steel Using Electron-Beam Surfacing and Investigation of Cutting Forces when Milling Workpieces. *Materials* **2023**, *16*, 4529. [CrossRef]
28. Oyelola, O.; Crawforth, P.; M'Saoubi, R.; Clare, A.T. Machining of functionally graded Ti6Al4V/WC produced by directed energy deposition. *Addit. Manuf.* **2018**, *24*, 20–29. [CrossRef]
29. Levano Blanch, O.; Suárez Fernández, D.; Graves, A.; Jackson, M. Mul Ti-FAST: A Machinability Assessment of Functionally Graded Titanium Billets Produced from Multiple Alloy Powders. *Materials* **2022**, *15*, 3237. [CrossRef]
30. Wang, C.; Ge, Y.; Ma, J.; Yu, Z.; Zhang, K.; Liu, T.; Guo, X.; Huang, S. Effects of parameter selection strategy on tool wear when milling 3D-printed functionally graded materials with textured tool under minimum quantity lubrication. *Int. J. Adv. Manuf. Technol.* **2023**, *125*, 1615–1632. [CrossRef]
31. Feenstra, D.R.; Cruz, V.; Gao, X.; Molotnikov, A.; Birbilis, N. Effect of build height on the properties of large format stainless steel 316L fabricated via directed energy deposition. *Addit. Manuf.* **2020**, *34*, 101205. [CrossRef]
32. Zhang, Q.L.; Yao, J.H.; Mazumder, J. Laser direct metal deposition technology and microstructure and composition segregation of Inconel 718 superalloy. *J. Iron Steel Res. Int.* **2011**, *18*, 73–78. [CrossRef]
33. Yan, S.; Wang, Y.; Wang, Q.; Zhang, C.; Chen, D.; Cui, G. Enhancing mechanical properties of the spark plasma sintered Inconel 718 alloy by controlling the nano-scale precipitations. *Materials* **2019**, *12*, 3336. [CrossRef] [PubMed]

34. Guiraldenq, P.; Duparc, O.H. The genesis of the Schaeffler diagram in the history of stainless steel. *Metall. Res. Technol.* **2017**, *114*, 613. [CrossRef]
35. Fortan, M.; Dejans, A.; Debruyne, D.; Rossi, B. The strength of stainless steel fillet welds using GMAW. In Proceedings of the Stainless Steel in Structures: Fifth International Experts Seminar, London, UK, 18–19 September 2017; pp. 1–13.
36. Liverani, E.; Toschi, S.; Ceschini, L.; Fortunato, A. Effect of selective laser melting (SLM) process parameters on microstructure and mechanical properties of 316L austenitic stainless steel. *J. Mater. Process. Technol.* **2017**, *249*, 255–263. [CrossRef]
37. Manikandan, S.G.K.; Sivakumar, D.; Rao, K.P.; Kamaraj, M. Effect of weld cooling rate on Laves phase formation in Inconel 718 fusion zone. *J. Mater. Process. Technol.* **2014**, *214*, 358–364. [CrossRef]